ACS OMEGA

http://pubs.acs.org/journal/acsodf

Article

Thermally Methanol Oxidation via the $Mn_1@Co_3O_4(111)$ Facet: Non-CO Reaction Pathway

Ju Wang,* Yusheng Liu, Wenchang Zhuang, Wenyou Zhu, Ju Huang, and Lin Tian*

Cite This: *ACS Omega* 2023, 8, 27293−27299

Read Online

ACCESS | Metrics & More | Article Recommendations | Supporting Information

ABSTRACT: Co_3O_4, as the support of single-atom catalysts, is effective in electron-structure modulation to get distinct methanol adsorption behaviors and adjustable reaction pathways for the methanol oxidation reaction. Herein, we considered the facets that constitute a Co vacancy of the $Co_3O_4(111)$ facet and a foreign metal atom M (M = Fe, Ni, Cu, Ru, Rh, Pd, Ag, Os, Ir, Pt, Au, Mn) leading to single-atom catalysts. The $Mn_1@Co_3O_4(111)$ facet is the facet considered the most favorable among all of the possible terminations. Oxygen adsorption, decomposition, and its co-adsorption with methanol are the vital steps of methanol oxidation at the exposed $Mn_1@Co_3O_4(111)$ facet, giving rise to the stable configuration: two O* and one CH_3OH* adsorbates. Then, the $Mn_1@Co_3O_4(111)$ facet activates the O−H and C−H bonds within CH_3OH*, advances CH_3O* → H_2CO* → HCOO* → COO*, and releases the products H_2, H_2O, and CO_2 consecutively.

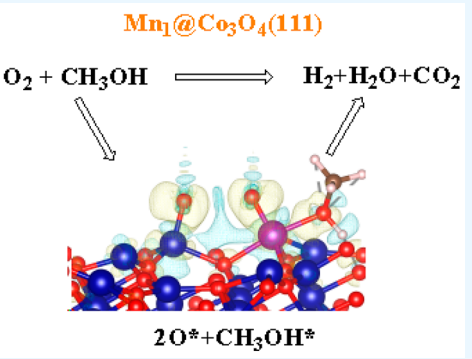

1. INTRODUCTION

Direct methanol fuel cells (DMFCs) have been regarded as one of the most prospective energy storage and conversion devices.[1] Efficient catalysts of the methanol oxidation reaction (MOR) are critical in the development of DMFCs.[2] In general, MOR catalytic systems are the oxides, nonoxides, and carbon-based catalysts.[3−5] Single-atom catalysts that offer the means of reducing the costs associated with preparation and utilization of noble metal catalysts have become promising alternatives for methanol oxidation reaction to address the bottleneck in low efficiency in the past decade.[6−8] Various single-atom catalysts for MOR were designed and synthesized.[9−11] Pt/α-MoC presented by Ma exhibited a particular efficiency for methanol aqueous-phase reforming, as well as the latter Ni/α-MoC.[12,13] Pd_1/Fe_3O_4, designed and synthesized by Rousseau,[14] preferred the excellent catalytic performance for partial oxidation of methanol. Rutile $Au_1@TiO_2$, especially its (110) facet, has been shown to be not only advantageous to direct methanol dehydrogenation but also available to partial oxidation of methanol.[15,16]

Co_3O_4, as the support of single-atom catalysts, is also superior in electron-structure modulation to induce the adjustments for methanol adsorption behaviors and reaction pathways.[17,18] The good performance of Co_3O_4-supported single-atom catalysts for MOR is probably derived from the reconstructed facets via the strategies of metal doping, diverse morphology, and defect engineering.[19,20] For instance, $Pt_1−Co_3O_4$ designed and synthesized by He[21] has preferred methanol oxidation to CO_2. It is found that the substitutional Pt sites with a large proportion of occupied high electronic states at the $Co_3O_4(111)$ facet increase the metal−support interactions and promote the co-adsorption of methanol and O_2 molecules.[21] However, it remains to be disclosed whether the reconstructed facets derived from metal doping and diverse morphologies contain the original defects of Co_3O_4. Moreover, how can the synergistic effect of metal doping, morphology adjustment, and surface defects have a distinct impact on methanol adsorption behaviors and oxidation reaction pathways? What kind of impact will oxygen stoichiometry environment have on the stability of single-atom catalysts? These are significant for understanding real active species in methanol oxidation reaction and developing highly efficient MOR catalysts.

Herein, we considered the facets that consist of one Co vacancy of the $Co_3O_4(111)$ facet and one foreign metal atom M (M = Mn, Fe, Ni, Cu, Ru, Rh, Pd, Ag, Os, Ir, Pt, Au) leading to single-atom catalysts. We find that the $Mn_1@Co_3O_4(111)$ facet is the one considered the most favorable among all of the possible terminations. Then, charge density difference and electronic local functions were performed to reveal the stability mechanism of the $Mn_1@Co_3O_4(111)$ facet and its modulation behaviors for the methanol oxidation reaction. Notably, oxygen adsorption and decomposition occur at the $Mn_1@Co_3O_4(111)$ facet earlier than methanol adsorption. Two competitive

Received: April 18, 2023
Accepted: July 10, 2023
Published: July 19, 2023

reaction pathways for oxygen decomposition are considered explicitly, namely, via bi-O_2* and O_2*. Then, methanol co-adsorption with two O* adsorbates and its non-CO reaction pathways at the $Mn_1@Co_3O_4(111)$ facet were investigated.

2. COMPUTATIONAL METHOD

All the geometric and electronic calculations were performed by using the periodic density functional theory code Vienna Ab initio Simulation Package (VASP).[22,23] The Perdew−Becke−Ernzerh functional and the generalized gradient approximation were applied to assess the exchange-correlation energies.[24] Ionic core deficiency was depicted by the projector-augmented wave pseudopotentials.[25−27] The cutoff energy has been given as 400 eV.[28] The convergence of energy and force calculations was 10^{-6} and 0.02 eV/Å, respectively. The U value of the Co-localized 3d electronic correlation was set to 3.0 eV.[29−31] K-points were set as 3 × 3 × 1 and 10 × 10 × 1 to carry out geometry optimization and electronic analysis calculations, respectively. The van der Waals interactions have been taken into considered by the Grimme (DFT+D3) method.[32,33] The transition states were identified by the CI-NEB method and verified via vibrational analysis calculations.[34,35]

Single-atom catalysts have been modeled by a six-atom layer in 2 × 2 periodic slabs of the $Co_3O_4(111)$ facet (168 atoms). A surface Co atom at the $Co_3O_4(111)$ facet was replaced by a dopant atom M (M = Mn, Fe, Co, Ni, Cu, Ru, Rh, Pd, Ag, Os, Ir, Pt, Au), and different doping positions and diverse oxygen environments were considered. The top four layers of the slab have been fully relaxed, along with the lower two layers fixed in their bulk positions. The vacuum gap was set as 15 Å to avoid interactions between the neighboring slabs. The SAC formation energy $H_f^{SAC} = E_{SAC} - E_{surf} - (E_{bulk}^{Co} - E_{bulk}^{M})$ reflects the process that a dopant atom institutes the Co site at the exposed $Co_3O_4(111)$ facet.[36] E_{SAC}, E_{surf}, E_{bulk}^{Co}, and E_{bulk}^{M} are the energies of the $M_1@Co_3O_4(111)$ facet, the $Co_3O_4(111)$ facet, the bulk Co, and the bulk foreign metal M, respectively. The adsorption energy (E_{ads}) of O_2, CH_3OH, and possible methanol oxidation intermediates at the $M_1@Co_3O_4(111)$ facet were carried out using the formula $E_{ads} = E_{(adsorbate/slab)} - E_{(slab)} - E_{(adsorbate)}$.[37] Respectively, the reaction energy (ΔE) and the energy barrier (E_a) were defined by the formula $\Delta E = E_{(P)} - E_{(R)}$ and $E_a = E_{(TS)} - E_{(R)}$.[38] The chemical potential $\mu_{(SAC)}$ was described as $\mu_{(SAC)} = [E_{(SAC)} - n_{(O)}\mu_{(O)} - n_{(Co3O4)}\mu_{(Co3O4)}] - [E_{(Co3O4)} + \mu_{(Mn)}]$.[39,40] The electron localization function (ELF)[41] was derived from ELF = $(1 + \chi_\sigma^2)^{-1}$. More computational details are supplied in the Supporting Information.

3. RESULTS AND DISCUSSION

3.1. Energetics of the $M_1@Co_3O_4(111)$ Facets. The substitutional $M_1@Co_3O_4(111)$ facets (M = Os, Ru, Fe, Mn) with a negative formation enthalpy difference are energetically favorable,[42] as shown by the SAC formation energy difference results listed in Figures 1 and SI-1. The formation enthalpy difference ΔH_f for the $Mn_1@Co_3O_4(111)$ facet is −2.28 eV, and those for the $M_1@Co_3O_4(111)$ facets (M = Os, Ru, Fe) are −0.48, −0.86, and −0.94 eV. Conversely, the substitution of a surface Co atom by a foreign atom with the positive formation enthalpy difference is energetically unfavorable,[43] such as the facets: $Au_1@Co_3O_4(111)$, $Ag_1@Co_3O_4(111)$, $Cu_1@Co_3O_4(111)$, $Pd_1@Co_3O_4(111)$, $Pt_1@Co_3O_4(111)$, $Ni_1@Co_3O_4(111)$, $Rh_1@Co_3O_4(111)$, and $Ir_1@Co_3O_4(111)$.

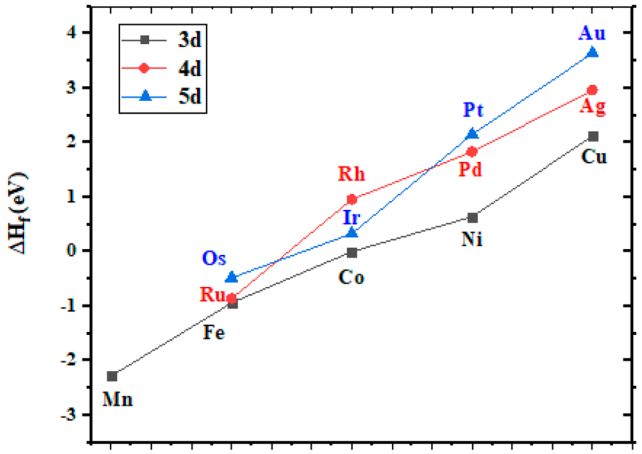

Figure 1. Enthalpy formation difference (ΔH_f) in eV for possible terminations of the $M_1@Co_3O_4(111)$ facets: M = Mn, Fe, Co, Ni, Cu, Ru, Rh, Pd, Ag, Os, Ir, Pt, Au. The black, red, and blue lines with squares, circles, and triangles represent the $M_1@Co_3O_4(111)$ facets doped with the 3d, 4d, and 5d valence orbital metal, respectively.

The $Mn_1@Co_3O_4(111)$ facet is the one considered the most favorable among all the possible terminations. As shown in Figure 2a,b, the substitutional Mn coordinates with three lattice oxygen atoms and three cobalt atoms. $Mn_1O_3Co_3$ represents its local environment. The lengths of the three Mn−O and three Mn−Co bonds are 1.777 1.777, 1.773, 2.387, 2.392, and 2.386 Å, respectively. An electron would transfer from the substitutional Mn to the lattice oxygen and cobalt atoms to form the stable Mn−O and Mn−Co bonds at the $Mn_1@Co_3O_4(111)$ facet, as presented in Figure 2c. The ELF values of Mn−O and Mn−Co are about 0.61 and 0.33, respectively. These results suggest that the substitutional Mn chemisorbed bonds to the surrounding oxygen and cobalt atoms on the exposed $Mn_1@Co_3O_4(111)$ facet.

Chemical potential results in Figures 2d and SI-2 indicate that surface oxygen vacancy occurs difficultly at the stable substitutional $Mn_1@Co_3O_4(111)$ facet, while oxygen adsorption onto its facet is energetically favorable. Under the typical catalyst calcination conditions ($\Delta\mu(O) = -0.78$ eV, 700 K), the $Mn_1@Co_3O_{4+2x}(111)$ and $Mn_1@Co_3O_{4+x}(111)$ terminations, the $Mn_1@Co_3O_4(111)$ facet with additional adsorbed oxygen atoms, are 15.76 and 10.34 eV more stable than the $Mn_1@Co_3O_4(111)$ one, respectively; the $Mn_1@Co_3O_{4-x}(111)$ and $Mn_1@Co_3O_{4-2x}(111)$ terminations, the $Mn_1@Co_3O_4(111)$ facet with oxygen vacancies, are 10.37 and 5.19 eV less stable than the $Mn_1@Co_3O_4(111)$ one, respectively. In addition, chemical potential results in Figures 2d and SI-2 also indicate that the supported $Mn_1/Co_3O_4(111)$ termination is energetically unfavorable, with an energy of 18.45 eV less stable than that of the substitutional $Mn_1@Co_3O_4(111)$ one under the typical catalyst calcination condition ($\Delta\mu(O) = -0.78$ eV, 700 K). More chemical potential results of $M_1@Co_3O_4(111)$ facets (M = Fe, Ru, Os) were presented in Figures SI-3−5.

3.2. Oxygen Adsorption, Decomposition, and Co-adsorption with Methanol at the $Mn_1@Co_3O_4(111)$ Facet. Oxygen adsorption, decomposition, and its co-adsorption with methanol are the vital steps of methanol oxidation at the exposed $Mn_1@Co_3O_4(111)$ facet. Oxygen adsorption and decomposition occur earlier than methanol adsorption. There are two stable adsorbate configurations

https://doi.org/10.1021/acsomega.3c02667
ACS Omega 2023, 8, 27293−27299

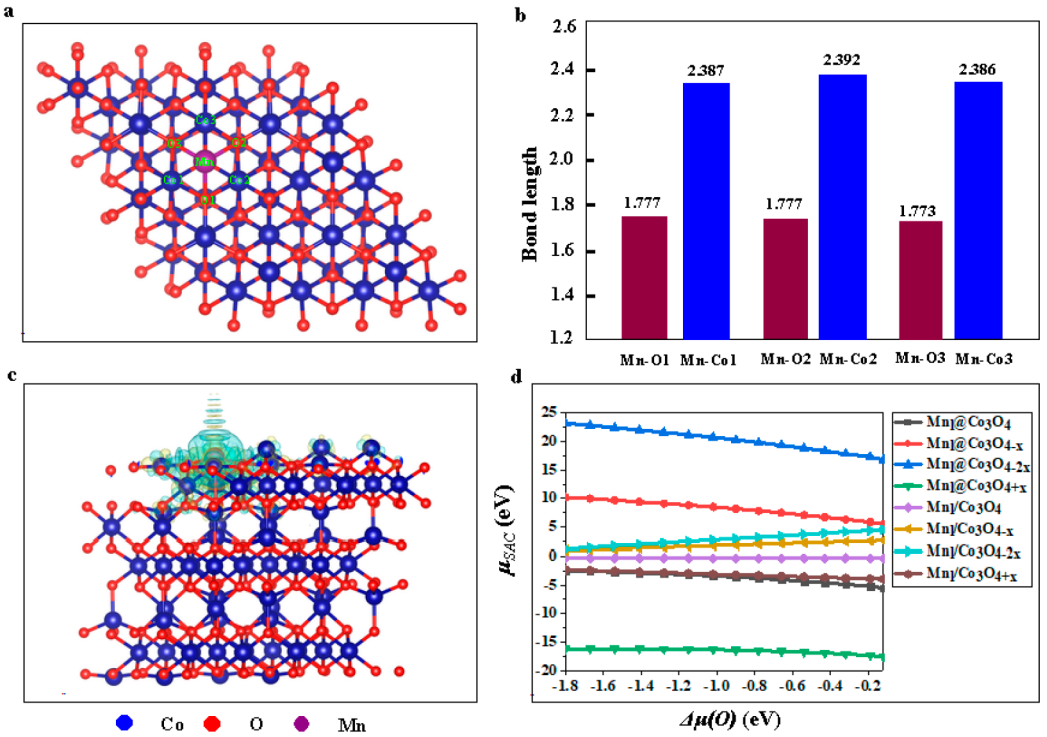

Figure 2. Stable substitutional $Mn_1@Co_3O_4(111)$ facet: (a) geometric structure (top view); (b) bond lengths of Mn−O and Mn−Co bonds; (c) charge difference density (side view); (d) chemical potential profiles of the $Co_3O_4(111)$ facet-based single-atom Mn catalysts.

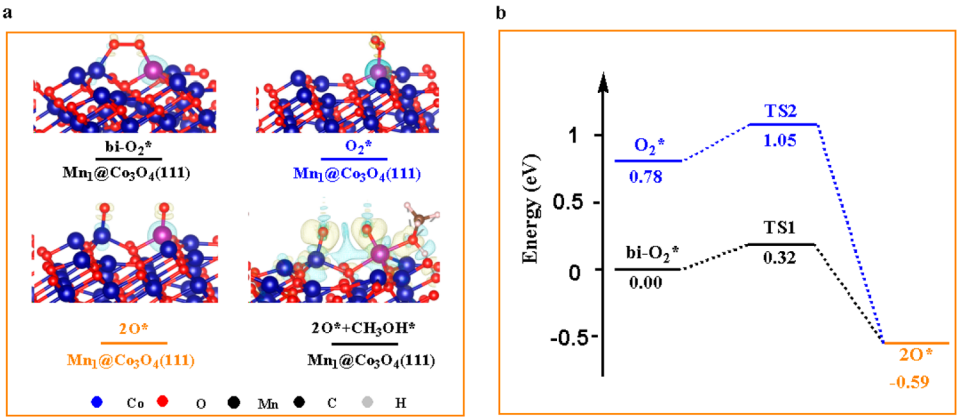

Figure 3. Oxygen adsorption, decomposition, and its co-adsorption with methanol at the exposed $Mn_1@Co_3O_4(111)$ facet: (a) charge density difference of the stable configurations; (b) the energy profile for oxygen decomposition.

when an oxygen molecule adsorbs onto the $Mn_1@Co_3O_4(111)$ facet, bi-O_2* and O_2*, as presented in Figure 3 and Table SI-1. Two competitive reaction pathways for oxygen decomposition are considered explicitly, namely, via bi-O_2* and O_2*.

The surface bi-O_2* adsorbate is energetically more favorable, with a lower system energy of −0.78 eV than that of O_2*. The adsorption energy (E_{ads}) between the adsorbate bi-O_2* and the $Mn_1@Co_3O_4(111)$ facet is −2.72 eV. An electron would transfer from the substitutional Mn to one oxygen atom of bi-O_2* to form the stable Mn−$O_{(bi\text{-}O2*)}$ bond, just as from the lattice Co atom to the other oxygen atom of bi-O_2* to form the stable Co−$O_{(bi\text{-}O2*)}$ bond, as presented in Figure 3a. Respectively, Mn−$O_{(bi\text{-}O2*)}$, Co−$O_{(bi\text{-}O2*)}$ and the lengths of the O−O are 1.741 1.791, and 1.443 Å. The adsorbate bi-O_2* decomposes on the $Mn_1@Co_3O_4(111)$ facet, leading to two O* adsorbates. This exothermic process requires a 0.32 eV barrier and 0.59 eV reaction energy (in Figure 3b), giving rise to the $Mn_1@Co_3O_{4+2x}(111)$ termination. For the adsorbate O_2*, the adsorption energy E_{ads} is −1.64 eV, with one oxygen atom bonding to the lattice Mn atom. The Mn−$O_{(O2*)}$ length is 1.730 Å. The adsorbate of O_2* can also decompose on the $Mn_1@Co_3O_4(111)$ facet, lead to two O* adsorbates, and give rise to the $Mn_1@Co_3O_{4+2x}(111)$ termination. Respectively, this exothermic process requires reaction energy and a barrier of 1.37 and 0.27 eV.

Then the methanol molecule adsorbs onto the surface Mn at the $Mn_1@Co_3O_{4+2x}(111)$ facet and leads to the adsorbate CH_3OH*. The charge density difference in Figure 3a shows that an electron would shift from the substitutional Mn to two oxygen atoms within the O* and CH_3OH* to form the stable Mn−O bonds. Meanwhile, the electron would transfer from the lattice Co to the oxygen atom within another O* to form

https://doi.org/10.1021/acsomega.3c02667
ACS Omega 2023, 8, 27293−27299

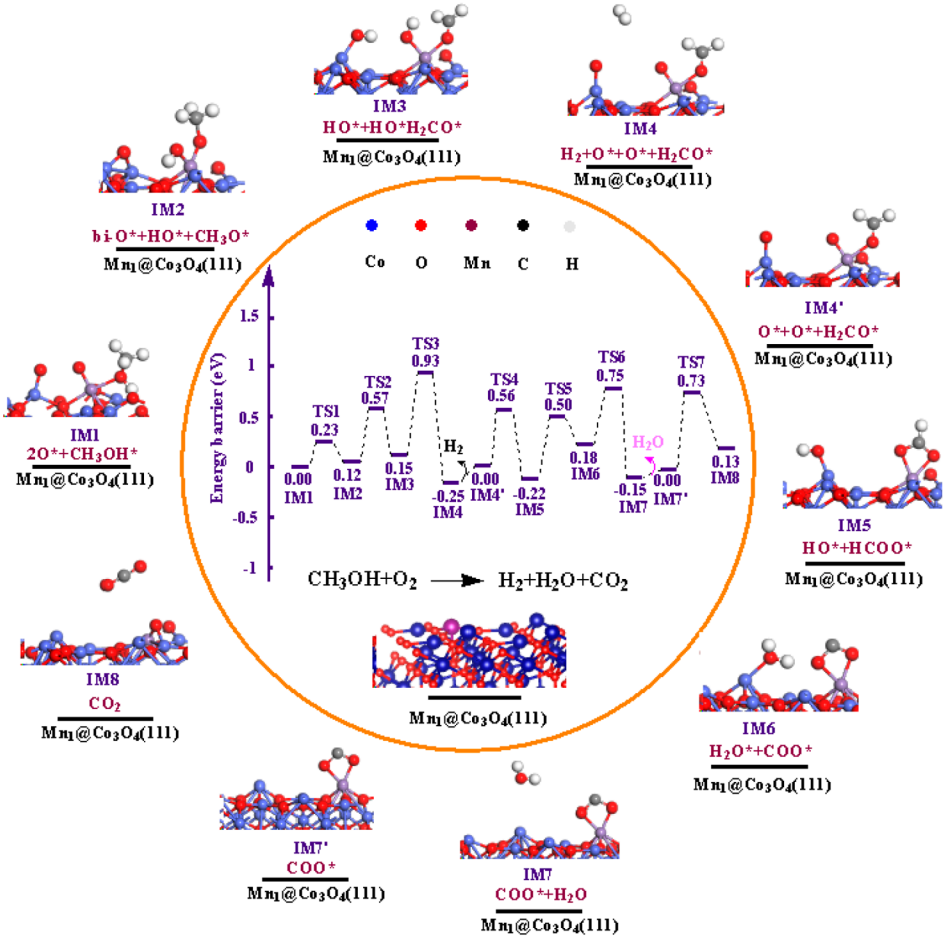

Figure 4. Methanol oxidation at the exposed $Mn_1@Co_3O_4(111)$ facet: possible reaction pathways and energy profile of the intermediates.

the stable Co−O bond. The lengths of Mn−$O_{(O^*)}$, Mn−$O_{(CH3OH^*)}$, and Co−$O_{(O^*)}$ are 1.741, 1.791, and 1.743 Å, respectively. The ELF values of Mn−$O_{(O^*)}$, Mn−$O_{(CH3OH^*)}$, and Co−$O_{(O^*)}$ are about 0.58, 0.62, and 0.51, respectively. Thus, the stable configuration of two O* adsorbates and their co-adsorption of methanol CH_3OH^* occurs at the exposed $Mn_1@Co_3O_4(111)$ facet.

3.3. Methanol Oxidation at the Exposed $Mn_1@Co_3O_4(111)$ Facet: Non-Co Pathway. We further studied the catalytic performance of the $Mn_1@Co_3O_4(111)$ facet for the methanol oxidation reaction. Notably, the $Mn_1@Co_3O_4(111)$ facet activates the O−H and C−H bonds within CH_3OH^*, advances the key adsorbates $CH_3O^* \rightarrow H_2CO^* \rightarrow HCOO^* \rightarrow COO^*$, and releases the products H_2, H_2O, and CO_2 separately.

As presented in Figure 4 and Table SI-2, for the initial O−H activation of CH_3OH^* and H transfer to one surficial $O_{(Mn)}^*$ on the $Mn_1@Co_3O_4(111)$ facet, a 0.23 eV barrier is required to form $CH_3O_{(Mn)}^*$ and $HO_{(Mn)}^*$ adsorbates within the intermediate IM2. Electron would transfer from the substitutional Mn to two oxygen atoms of $HO_{(Mn)}^*$ and $CH_3O_{(Mn)}^*$ adsorbates to construct two stable Mn−O bonds on the $Mn_1@Co_3O_4(111)$ facet, as presented in Figure 5a. The lengths of Mn−$O_{(HO^*)}$ and Mn−$O_{(CH3O^*)}$ bonds are 1.790 and 1.763 Å, respectively. In the meantime, the other surficial bi-$O_{(Co)}^*$ is bonded to two lattice Co atoms at the exposed $Mn_1@Co_3O_4(111)$ facet.

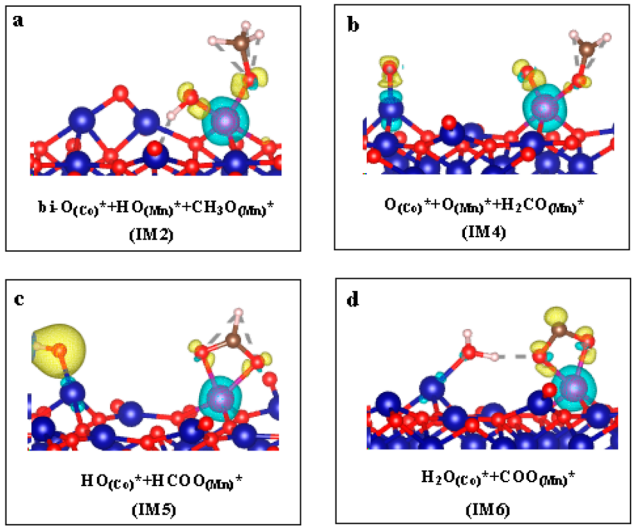

Figure 5. Charge density difference of the key adsorbates at the $Mn_1@Co_3O_4(111)$ facet in MOR: (a) bi-$O_{(Co)}^*$, $HO_{(Mn)}^*$, and $CH_3O_{(Mn)}^*$ within the intermediate IM2; (b) $O_{(Co)}^*$, $O_{(Mn)}^*$, and $H_2CO_{(Mn)}^*$ within the intermediate IM4. (c) $HO_{(Co)}^*$ and $HCOO_{(Mn)}^*$ within the intermediate IM5; (d) $H_2O_{(Co)}^*$ and $COO_{(Mn)}^*$ within intermediate IM6. The blue, red, purple, gray, and brown balls refer to Co, O, Mn, H, and C atoms, respectively.

https://doi.org/10.1021/acsomega.3c02667
ACS Omega 2023, 8, 27293−27299

Then, C−H activation occurs on the $CH_3O_{(Mn)}$* adsorbate of intermediate IM2, which further releases H_2 and H_2O from the facet consecutively. For the first C−H activation, a 0.45 eV energy barrier is required to give rise to $H_2CO_{(Mn)}$* adsorbate; meanwhile, H transfers to the other surficial bi-$O_{(Co)}$* at the exposed $Mn_1@Co_3O_4(111)$ facet to form the $HO_{(Co)}$* adsorbate. The H_2 release step occurs upon the surficial $HO_{(Co)}$* and $HO_{(Mn)}$* adsorbates, which is favorable with a 0.78 eV barrier and leads to the intermediate IM4 with the adsorbates $H_2CO_{(Mn)}$*, $O^*_{(Mn)}$, and $O^*_{(Co)}$. As presented in Figure 5b, electrons would transfer from the substitutional Mn to two oxygen atoms of the $O_{(Mn)}$* and $H_2CO_{(Mn)}$* adsorbates to form two stable Mn−O bonds, as well as that from the lattice Co to the oxygen atom of the $O_{(Co)}$* adsorbate to form the stable Co−O bond.

The second C−H activation occurring upon the adsorbate $H_2CO_{(Mn)}$* requires a 0.56 eV energy barrier and leads to $HCOO_{(Mn)}$* and $HO^*_{(Co)}$ adsorbates within the intermediate IM5. Especially, the adsorbate $HCOO_{(Mn)}$* is derived from the bonding between $O^*_{(Mn)}$ and $HCO_{(Mn)}$* after C−H activation occurred on the adsorbate $H_2CO_{(Mn)}$*; meanwhile, H transfers to $O^*_{(Co)}$ to form $HO^*_{(Co)}$. An electron would transfer from the substitutional Mn to two oxygen atoms within the $HCOO_{(Mn)}$* adsorbate to form two stable Mn−$O_{(HCOO^*)}$ bonds (Figure 5c), as well as that from the lattice Co atom to the adsorbate $HO^*_{(Co)}$. The ELF values of two Mn−$O_{(HCOO^*)}$ bonds and one Co−$O_{(HO^*)}$ bond are about 0.61, 0.58, and 0.41, respectively, as well as their lengths being 1.958, 1.887, and 1.750 Å, respectively.

The third C−H activation occurring upon the adsorbate $HCOO_{(Mn)}$* requires a 0.72 eV energy barrier and leads to $COO_{(Mn)}$* and $H_2O^*_{(Co)}$ adsorbates within the intermediate IM6, the key intermediate for methanol oxidation at the exposed $Mn_1@Co_3O_4(111)$ facet. An electron would transfer from the substitutional Mn to two oxygen atoms within the $COO_{(Mn)}$* adsorbate to form two Mn−$O_{(COO^*)}$ bonds presented in Figure 5d as well as that from the lattice Co atom to the oxygen atom of the $H_2O_{(Co)}$* adsorbate to form one Co−$O_{(H2O^*)}$ bond. The adsorption energy for the adsorbate $H_2O_{(Co)}$* at the exposed $Mn_1@Co_3O_4(111)$ facet is −1.07 eV, and that for $COO_{(Mn)}$* is −1.28 eV. The *ELF* values of two Mn−$O_{(COO^*)}$ bonds and one Co−$O_{(H2O^*)}$ bond are about 0.41, 0.39, and 0.21, respectively, weaker than those in the intermediate IM5. The lengths of two Mn−$O_{(COO^*)}$ bonds and one Co−$O_{(H2O^*)}$ bond are 1.971, 2.018, and 1.989 Å, respectively. All of these are favorable for the subsequent H_2O and CO_2 desorption from the facet. H_2O desorption occurs earlier. This process requires a 0.57 eV energy barrier and gives rise to the $COO_{(Mn)}$* adsorbate within the intermediate IM7. The adsorption energy for $COO_{(Mn)}$* is −0.95 eV. Two Mn−$O_{(COO^*)}$ lengths are 1.978 and 1.878 Å, respectively. Finally, CO_2 releases from the $Mn_1@Co_3O_4(111)$ facet after overcoming the 0.73 eV energy barrier.

4. CONCLUSIONS

In summary, we considered the facets that consist of one Co vacancy of the $Co_3O_4(111)$ facet and one foreign atom M (M = Mn, Fe, Ni, Cu, Ru, Rh, Pd, Ag, Os, Ir, Pt, Au) leading to single-atom catalysts. The $Mn_1@Co_3O_4(111)$ facet is the one considered the most favorable among all the possible terminations. The substitutional Mn atom is chemisorbed and bonded with three lattice oxygen atoms and three lattice cobalt atoms. $Mn_1O_3Co_3$ represents its local environment. Oxygen adsorption, decomposition, and its co-adsorption with methanol are the vital steps of methanol oxidation at the exposed $Mn_1@Co_3O_4(111)$ facet. Two competitive reaction pathways for oxygen decomposition, bi-O_2* and O_2*, are considered explicitly, which further gives rise to the two O* adsorbates at the $Mn_1@Co_3O_4(111)$ facet. Then, the methanol molecule adsorbs onto the facet and leads to the stable adsorbates: two O* and CH_3OH*. Furthermore, the $Mn_1@Co_3O_4(111)$ facet activates O−H and C−H within CH_3OH*, advances the key adsorbates $CH_3O^* \rightarrow H_2CO^* \rightarrow HCOO^* \rightarrow COO^*$, and releases H_2, H_2O, and CO_2 consecutively.

■ ASSOCIATED CONTENT

Supporting Information

The Supporting Information is available free of charge at https://pubs.acs.org/doi/10.1021/acsomega.3c02667.

Computational details and DFT calculation results for chemical potentials $\mu_{(SAC)}$, the adsorption energy E_{ads}, the reaction energy ΔE, the energy barrier E_a, and the electron localization function ELF (Figures SI-1−5), as well as the partial configuration data for the key intermediates of methanol oxidation at the $Mn_1@Co_3O_4(111)$ facet (Tables S1 and S2) (PDF)

■ AUTHOR INFORMATION

Corresponding Authors

Ju Wang − *School of Materials and Chemical Engineering, Xuzhou University of Technology, Xuzhou 221018, P.R. China*; orcid.org/0000-0001-8619-0367; Email: wangju@xzit.edu.cn

Lin Tian − *School of Materials and Chemical Engineering, Xuzhou University of Technology, Xuzhou 221018, P.R. China*; orcid.org/0000-0002-4345-5414; Email: xzittl@xzit.edu.cn

Authors

Yusheng Liu − *School of Materials and Chemical Engineering, Xuzhou University of Technology, Xuzhou 221018, P.R. China*

Wenchang Zhuang − *School of Materials and Chemical Engineering, Xuzhou University of Technology, Xuzhou 221018, P.R. China*

Wenyou Zhu − *School of Materials and Chemical Engineering, Xuzhou University of Technology, Xuzhou 221018, P.R. China*

Ju Huang − *School of Materials and Chemical Engineering, Xuzhou University of Technology, Xuzhou 221018, P.R. China*

Complete contact information is available at: https://pubs.acs.org/10.1021/acsomega.3c02667

Notes

The authors declare no competing financial interest.

■ ACKNOWLEDGMENTS

This work was supported by the National Natural Science Foundation of China (Grant No. 21703194).

■ REFERENCES

(1) Lu, W. Q.; Zhang, R. J.; Toan, S.; Xu, R.; Zhou, F. Y.; Sun, Z.; Sun, Z. Q. Microchannel structure design for hydrogen supply from methanol steam reforming. *Chem. Eng. J.* **2022**, *429*, 132286.

(2) Chen, L.; Liang, X.; Wang, D. S.; Yang, Z. B.; He, C. T.; Zhao, W.; Pei, J. J.; Xue, Y. R. Platinum-ruthenium single atom alloy as a bifunctional electrocatalyst toward methanol and hydrogen oxidation reactions. *ACS Appl. Mater. Interfaces* **2022**, *14*, 27814−27822.
(3) Sha, F.; Han, Z.; Tang, S.; Wang, J. J.; Li, C. Hydrogenation of carbon dioxide to methanol over non-Cu-based heterogeneous catalysts. *ChemSusChem* **2020**, *13*, 6160−6181.
(4) Chen, W. H.; Chen, K. H.; Lin, B. J.; Guo, Y. Z. Catalyst combination strategy for hydrogen production from methanol partial oxidation. *Energy* **2020**, *206*, 118180.
(5) Morales-Leal, F. J.; Rivera De La Rosa, J. R.; Lucio-Ortiz, C. J.; Del Rio, D. A. D.; Garza-Navarro, M. A.; Tian, W.; Herrera, J. E. Monometallic platinum and palladium-based catalysts in the competitive oxidation of methanol over the liquid-phase methanol-ethanol mixtures. *Chem. Eng. J.* **2021**, *426*, 131623.
(6) Zhang, Z. Q.; Liu, Z. P.; Wang, J.; Wang, Q.; Wang, Y. H.; Wang, K.; Wang, Z.; Gu, M.; Tang, Z. H.; Lim, J. Single-atom catalyst for high-performance methanol oxidation. *Nat. Commun.* **2021**, *12*, 5235.
(7) Lu, Y. B.; Zhang, Z. H.; Wang, H. M.; Wang, Y. Toward efficient single-atom catalysts for renewable fuels and chemicals production from biomass and CO_2. *Appl. Catal., B* **2021**, *292*, 120162.
(8) Jeong, H. J.; Shin, D. J.; Kim, B. S.; Bae, J. M.; Shin, S. Y.; Choe, C. Y.; Han, J. W.; Lee, H. Controlling the oxidation state of Pt single atoms for maximizing catalytic activity. *Angew. Chem., Int. Ed.* **2020**, *59*, 20691−20696.
(9) He, H.; Wang, H. H.; Liu, J. J.; Liu, X. J.; Li, W. Z.; Wang, Y. N. Research progress and application of single-atom catalysts: a review. *Molecules* **2021**, *26*, 6501.
(10) Zhang, L. N.; Xue, L. L.; Lin, B. Y.; Zhao, Q. G.; Wan, S. L.; Wang, Y.; Jia, H. P.; Xiong, H. F. Noble metal single-atom catalysts for the catalytic oxidation of volatile organic compounds. *ChemSusChem* **2022**, *15*, No. e202102494.
(11) Lang, R.; Xi, W.; Liu, J. C.; Cui, Y. T.; Li, T. B.; Lee, A. F.; Chen, F.; Chen, Y.; Li, L.; Lin, J.; Miao, S.; Liu, X. Y.; Wang, A. Q.; Wang, X. D.; Luo, J.; Qiao, B. T.; Li, J.; Zhang, T. Non defect-stabilized thermally stable single-atom catalyst. *Nat. Commun.* **2019**, *10*, 234.
(12) Lin, L. L.; Yu, Q. L.; Peng, M.; Li, A. W.; Yao, S. Y.; Tian, S. H.; Liu, X.; Li, A.; Jiang, Z.; Gao, R.; Han, X. D.; Li, Y. W.; Wen, X. D.; Zhou, W.; Ma, D. Atomically dispersed Ni/alpha-MoC catalyst for hydrogen production from methanol/water. *J. Am. Chem. Soc.* **2021**, *143*, 309−317.
(13) Lin, L. L.; Zhou, W.; Gao, R.; Yao, S. Y.; Zhang, X.; Xu, W. Q.; Zheng, S. J.; Jiang, Z.; Yu, Q. L.; Li, Y. W.; Shi, C.; Wen, X. D.; Ma, D. Low-temperature hydrogen production from water and methanol using Pt/alpha-MoC catalysts. *Nature* **2017**, *544*, 80−83.
(14) Marcinkowski, M. D.; Yuk, S. F.; Doudin, N.; Smith, R. S.; Nguyen, M. T.; Kay, B. D.; Glezakou, V. A.; Rousseau, R.; Dohnalek, Z. Low-temperature oxidation of methanol to formaldehyde on a model single-atom catalyst: Pd atoms on Fe_3O_4 (001). *ACS Catal.* **2019**, *9*, 10977−10982.
(15) Wang, J.; Zhang, W.; Zhu, W. Y.; Zhuang, W. C.; Lei, M. Rutile TiO_2 supported single-atom Au catalyst: a facile approach to enhance methanol dehydrogenation. *Mol. Catal.* **2020**, *482*, 110670.
(16) Wang, J.; Lei, M.; Wang, Z. X.; Liu, Y. S.; Zhuang, W. C.; Zhu, W. Y. Methanol oxidation over rutile Au_1@TiO_2 catalyst: importance of facets and oxygen vacancy. *Appl. Surf. Sci.* **2021**, *542*, 148541.
(17) Zhu, W. J.; Wang, X. B.; Li, C.; Chen, X.; Li, W. Y.; Li, Z. M.; Liang, C. H. Defect engineering over Co_3O_4 catalyst for surface lattice oxygen activation and boosted propane total oxidation. *J. Catal.* **2022**, *413*, 150−162.
(18) Chu, B. X.; Liu, X. Q.; Qin, Q. J.; Zhao, R. Q.; Chen, K. A.; Hou, X. Y.; Li, R. Y.; Li, C.; Dong, L. H.; Li, B. Surface cleaning and protection engineering via functionalization to awaken the intrinsic catalytic activity of Co_3O_4. *Adv. Funct. Mater.* **2023**, *33*, 2212448.
(19) Zhao, S.; Yang, H.; Liu, Y. R.; Xing, Y. D.; Cui, G. W.; Liu, Q. Y. Cu-doped Co_3O_4 microstructure as an efficient non-noble metal electrocatalyst for methanol oxidation in a basic solution. *New J. Chem.* **2021**, *45*, 11245−11252.
(20) Zhang, Y.; Sun, Y. B.; Cai, Z.; You, S. J.; Li, X. R.; Zhang, Y. H.; Yu, Y.; Ren, N. Q.; Zou, J. L. Stable CuO with variable valence states cooperated with active Co^{2+} as catalyst/co-catalyst for oxygen reduction/methanol oxidation reactions. *J. Colloid Interface Sci.* **2021**, *593*, 345−358.
(21) Jiang, Z. Y.; Feng, X. B.; Deng, J. L.; He, C.; Douthwaite, M.; Yu, Y. K.; Liu, J.; Hao, Z. P.; Zhao, Z. Atomic-scale insights into the low-temperature oxidation of methanol over a single-atom Pt_1-Co_3O_4 catalyst. *Adv. Funct. Mater.* **2019**, *29*, 1902041.
(22) Kresse, G.; Hafner, J. Ab initio molecular dynamics for liquid metals. *Phys. Rev. B Condens Matter* **1993**, *47*, 558−561.
(23) Hafner, J. Ab-initio simulation of materials using VASP: density-functional theory and beyond. *J. Comput. Chem.* **2008**, *29*, 2044−2078.
(24) Perdew, J. P.; Burke, K.; Ernzerhof, M. Generalized gradient approximation made simple. *Phys. Chem. Lett.* **1996**, *77*, 3865−3868.
(25) Kresse, G.; Furthmller, J. Efficiency of ab-initio total-energy calculations for metals and semiconductors using a plane-wave basis set. *Comput. Mater. Sci.* **1996**, *6*, 15−50.
(26) Kresse, G.; Furthmller, J. Efficient iterative schemes for ab initio total-energy calculations using a plane-wave basis set. *Phys. Chem. B Condens. Matter.* **1996**, *54*, 11169−11186.
(27) Kresse, G.; Joubert, D. From ultrasoft pseudopotentials to the projector augmented-wave method. *Phys. Rev. B* **1999**, *59*, 1758−1775.
(28) Lv, C. Q.; Liu, C.; Wang, G. C. A DFT study of methanol oxidation on Co_3O_4. *Catal. Commun.* **2014**, *45*, 83−90.
(29) Anisimov, V. L.; Aryasetiawan, F.; Lichtenstein, A. I. First-principles calculations of the electronic structure and spectra of strongly correlated systems: the LDA+U method. *J. Phys.: Condens. Matter.* **1997**, *9*, 767−808.
(30) Dudarev, S. L.; Botton, G. A.; Savrasov, S. Y.; Humphreys, C. J.; Sutton, A. P. Electronic-energy-loss spectra and the structural stability of nickel oxide: an LSDA+U study. *Phys. Rev. B* **1998**, *57*, 1505−1509.
(31) Brown, J. J.; Page, A. J. The Hubbard-U correction and optical properties of d^0 metal oxide photocatalysts. *J. Chem. Phys.* **2020**, *153*, 224116.
(32) Grimme, S.; Ehrlich, S.; Georigk, L. Effect of the damping function in dispersion corrected density functional theory. *J. Chem. Phys.* **2011**, *32*, 1456−1465.
(33) Grimme, S.; Antony, J.; Ehrlich, S.; Krieg, H. A consistent and accurate ab initio parameterization of density functional dispersion correction (DFT-D) for the 94 elements H-Pu. *J. Chem. Phys.* **2010**, *32*, No. 154104.
(34) Mills, G.; Jonsson, H.; Schenter, G. K. Reversible work transition state theory: application to dissociative adsorption of hydrogen. *Surf. Sci.* **1995**, *324*, 305−327.
(35) Henkelman, G.; Uberuaga, B. P.; Jonsson, H. A climbing image nudged elastic band method for finding saddle points and minimum energy paths. *J. Chem. Phys.* **2000**, *113*, 9901−9904.
(36) Mahlberg, D.; Grob, A. Vacancy assisted diffusion on single-atom surface alloys. *ChemPhysChem.* **2021**, *22*, 29−29.
(37) Zhang, W.; Pu, M.; Lei, M. Theoretical studies on stability and reactivity of metals doped CeO_2 (100) surface: towards H_2 dissociation and oxygen vacancy formation. *Langmuir* **2020**, *36*, 5891−5901.
(38) Yue, C. W.; Wang, L. C.; Wang, H. H.; Du, J. R.; Lei, M.; Pu, M. First-principles study on the electrocatalytic oxygen evolution reaction on the (110) surfaces of layered double hydroxides. *J. Phys. Chem. C* **2022**, *126*, 18351−18365.
(39) Tang, Y.; Asokan, C.; Xu, M.; Graham, G. W.; Pan, X.; Christopher, P.; Li, J.; Sautet, P. Rh single atoms on TiO_2 dynamically respond to reaction conditions by adapting their site. *Nat. Commun.* **2019**, *10*, 4488.
(40) Machrafi, H. On the chemical potential of nanoparticle dispersion. *Phys. Lett. A* **2020**, *384*, 126485.
(41) Savin, A.; Nesper, R.; Wengert, S.; Fassler, T. F. EFL: the electron localization function. *Angew. Chem. Int. Engl.* **1997**, *36*, 1808−1832.

https://doi.org/10.1021/acsomega.3c02667
ACS Omega 2023, 8, 27293−27299

(42) Gohda, Y.; Gross, A. Local reactivity of ultrathin platinum overlayers and surface alloys on a gold surface. *Surf. Sci.* **2007**, *601*, 3702−3706.
(43) Gohda, Y.; Gross, A. Structure-reactivity relationship for bimetallic electrodes: Pt overlayers and PtAu surface alloys on Au(111). *J. Electroanal. Chem.* **2007**, *607*, 47−53.

https://doi.org/10.1021/acsomega.3c02667
ACS Omega 2023, 8, 27293−27299